# Reducing source wavelet non-repeatability for time-lapse shot gathers

Xin Fu and Kris Innanen


## ABSTRACT

In time-lapse seismic surveys, the effective seismic signals produced by property changes of subsurface rocks are often ruined by non-repeatability noises. In this paper, starting from the wave equation, base on the relationship between wavefields and Green's functions, we propose two frequency-domain matching filters to reduce source wavelet non-repeatability for time-lapse shot gathers, one is the spectrum ratio of the baseline and monitoring wavelets, the other one is the average spectrum ratio of the baseline and monitoring traces. The former requires the wavelets information of baseline and monitoring data, and the latter is source-independent. After reducing the source wavelet non-repeatability, we employ time-shifts corrections by a fast local cross-correlations algorithm to further reduce non-repeatability errors in the difference data (monitoring data minus baseline data) that caused by time shifts between monitoring and baseline data. And then, a reverse time migration (RTM) in depth with a Poynting Vector imaging condition used to reduce the remaining errors arising from the inaccuracy of the source-independent matching filter is carried out. The feasibility of our methods is demonstrated by the synthetic noise-free and noisy data tests. The spectrum ratio of the baseline and monitoring wavelets can effectively solve the source wavelet non-repeatability issue. The source-independent filter also shows good performance in these tests.


## INTRODUCTION

Time-lapse or 4D seismic analysis as a crucial technology has been employed in reservoir monitoring (e.g., enhanced oil recovery and/or $CO_2$ storage problems) and characterization for decades (Greaves and Fulp, 1987; Ross and Altan, 1997; Wang et al., 1998; Barkved et al., 2003; Arts et al., 2003; Barkved et al., 2005; Chadwick et al., 2009; Kazemeini et al., 2010; Pevzner et al., 2017). It has begun to be incorporated into the development plan of each reservoir (Jack, 2017). In 3D or single-time seismic data, the information about the static geology and that about the dynamic fluid flow are interweaved, whereas, the time-lapse seismic data, including two or more datasets obtained at different times, can rid off the time-invariant signal corresponding to the geology part and directly reflects time-variant fluid-flow changes (Lumley, 2001). Although time-lapse seismic technology is of such good merit theoretically, it is often disturbed by many issues.

These issues can be categorized into three types. The first is the geology changing issues. During the oil/gas production and/or fluid injection (water, gas, steam, CO2, etc.), reservoir subsidence, compaction, porosity, or/and overburden pressure changes could happen. The second is the non-repeatability issues, including acquisition non-repeatability and processing non-repeatability. The acquisitions carried out at different times can be different in environment (noise conditions, near-surface properties, water table, seawater properties, seal level, weather, etc.), geometry (source and receiver positions, etc.), receiver equipment, and source wavelet. The processing non-repeatability can be caused by different

processors, different processing parameters, and different workflows. The third is the issue of intrinsic errors. Even for twice surveys (baseline and monitoring surveys) with the constant geology and perfect acquisition and processing repeatability, errors still occur in time-lapse imaging (monitoring imaging minus baseline imaging), since the subsurface property change arises both travel time (kinetic) and amplitude (dynamic) differences in both reservoir and non-reservoir zones between baseline and monitoring seismic data. However, the most we want is the seismic amplitude change in the reservoir zone, although time shifts (travel time differences) between monitoring and baseline data can also provide some useful information about the reservoir (Hatchell and Bourne, 2005).

Geology changing issues are reported in some places, for instance, the North Sea case (Hicks et al., 2016) and the Valhall Field case (Hall et al., 2005). As for the non-repeatability issues of the acquisition environment, they are hard to be solved, since they are unrepeatable or out of our control. We can only decrease the impact of some, for example, carrying out the acquisitions in the same season, installing the receivers on the sea bed or permanently on land.

The most typical technique is the cross-equalization (Ross et al., 1996), a synthetical method reducing errors caused by nonrepeatable seismic acquisition and processing. Tucker et al. (2000) use a time-domain least-squares or optimum Wiener matching filter to implement the cross-equalization. Al-Ismaili and Warner (2002) perform the cross-equalization by artifactial neural networks. Gallop (2011) presents midpoint match filters for time-lapse seismic data matching. Almutlaq and Margrave (2013) evaluate the concept of surface-consistent matching filters to handle time-lapse seismic data with nonrepeatable acquisition parameters. Bergmann et al. (2014) propose a static correction method to reduce differences in reflection travel times of time-lapse prestack seismic data. Hatchell and Tatanova (2019) conclude that the spectral balancing filter has better anti-noise capacity than the standard time-domain least-squares filter after the comparison between them.

Rickett and Lumley (2001) introduce warping as a residual migration operator to colocate reflectors imaged at different positions to alleviate residual errors after doing cross-equalization. Hale (2006, 2013) proposes two popular algorithms, fast local cross-correlations, and dynamic warping, for seismic image registration. He also estimates three-component apparent displacement vectors from time-lapse seismic images, using local phase correlations and a cyclic sequence of searches for peaks of correlations (Hale, 2009). In Fomel and Jin (2009), the local similarity attribute (Fomel, 2007) are applied for time-lapse seismic image registration. Based on their work, an improved version is developed by Liu et al. (2021). Other warping approchs you can see in Williamson et al. (2007), Phillips and Fomel (2016), Karimi et al. (2016), and Dramsch et al. (2019).

In our work, we start from the wave equation, base on the relationship between wavefields and Green's functions, propose two frequency-domain matching filters to reduce source wavelet non-repeatability for time-lapse shot gathers. One requires the wavelets information of baseline and monitoring data, and the other one is source-independent. After reducing the source wavelet non-repeatability, we employ a time-shifts correction by a fast local cross-correlations algorithm (Hale, 2006) to further reduce non-repeatability errors caused by the time shifts in the difference data. And then, a reverse time migration (RTM)

in depth with a Poynting Vector imaging condition is used to reduce the remaining errors arising from the inaccuracy of the source-independent matching filter.

## THEORY

The main aim of time-lapse seismic processing is to eliminate the nonrepeatibility errors between baseline and monitoring datasets. In this section, we propose two matching filters to solve the source wavelet nonrepeatibility issue. One of them is source-independent. Then we abstract local time shifts between two datasets by a fast local cross-correlations algorithm. Finally, after decreasing the time shifts between two datasets, an RTM in depth with a Poynting Vector imaging condition is applied to image the difference data.

### Matching filters

According to the wave equation, for instance, a 2D constant-density acoustic wave equation:

$$\frac{\partial^2 P(x,z,t)}{\partial x^2}+\frac{\partial^2 P(x,z,t)}{\partial z^2}-\frac{1}{c^2(x,z)}\frac{\partial^2 P(x,z,t)}{\partial t^2}=w(t)\delta(x-x_0)\delta(z-z_0), \quad (1)$$

where $P(x,z,t)$ is the wavefield depending on coodinates $(x,z)$ and propagating time $t$, $c(x,z)$ is the P-wave velocity field depending on $(x,z)$, and $w(t)$ is the time-dependent source wavelet at location $(x_0,z_0)$. Then, the seismic data (the wavefields recorded by seismic receivers) can be expressed as convolutions of the Green's functions and the source wavelets:

$$d_{i,j}(t)=w_i(t)*g_{i,j}(t), \quad (2)$$

where $*$ denotes the convolution operator; subscripts $i$ and $j$ are shot number and receiver number, respectively; $d_{i,j}(t)$ is the observed seismic trace of shot $i$ at receiver $j$, and $g_{i,j}(t)$ is the corresponding Green's function; $w_i(t)$ is the source wavelet of shot $i$, which is the same for all traces in the same shot; all parameters depend on sampling time $t$. For a time-lapse survey, we use subscripts 1 and 2 for baseline and monitoring surveys, respectively, then we have the baseline seismic trace:

$$d_{1i,j}(t)=w_{1i}(t)*g_{1i,j}(t), \quad (3)$$

and the monitoring seismic trace:

$$d_{2i,j}(t)=w_{2i}(t)*g_{2i,j}(t). \quad (4)$$

In the case of baseline wavelet $w_{1i}(t)$ equals to monitoring wavelet $w_{2i}$, differencese between baseline and monitoring datasets are only generated by differences of the Green's functions that are related to the subsurface physical property change. But when $w_{1i}(t)$ is different from $w_{2i}$, the difference data are linked to both the source wavelet nonrepeatibility and the property change. A solution for the source wavelet nonrepeatibility issue is the double-wavelet method presented by Fu et al. (2020), constructing a common wavelet, $w_{1i}(t)*w_{2i}(t)$, by convolving baseline wavelet with monitoring trace and convolving monitoring wavelet with baseline trace. Hereon, we formulate a new method to eliminate the source wavelet nonrepeatibility.

The new method is formulated in frequency domain. First, we convert equation 3 and 4 into frequency domain by the Fourier transfer, then we have baseline seismic trace:

$$\hat{d}_{1i,j}(\omega) = \hat{w}_{1i}(\omega)\hat{g}_{1i,j}(\omega), \tag{5}$$

and monitoring seismic trace:

$$\hat{d}_{2i,j}(\omega) = \hat{w}_{2i}(\omega)\hat{g}_{2i,j}(\omega), \tag{6}$$

where $\omega$ is frequency and the "$\hat{}$" denotes the Fourier transform. The convolution in time domain corresponds to multiplication in frequency domain. We eliminate the source wavelet nonrepeatibility by multiplying a frequency-domain matching filter,

$$f_w(\omega) = \hat{w}_{1i}(\omega)/\hat{w}_{2i}(\omega), \tag{7}$$

with $\hat{d}_{2i,j}(\omega)$, then the filtered monitoring trace becomes:

$$\hat{d}'_{2i,j}(\omega) = f_w(\omega)\hat{d}_{2i,j}(\omega) = \hat{w}_{1i}(\omega)\hat{g}_{2i,j}(\omega), \tag{8}$$

where it has the same wavelet as the baseline trace. However, constructing the double wavelet $w_{1i}(t) * w_{2i}(t)$ and the matching filter $f_w(\omega)$ both require that baseline and monitoring wavelets are known. In this study, we think further and formulate a source-independent matching filter to reduce the source wavelet nonrepeatibility.

The source-independent matching filter, $f_s(\omega)$, is calculated from the average spectrum ratio of the baseline and monitoring traces, expressed as:

$$f_s(\omega) = \frac{1}{N}\sum_{i=1}^{ns}\sum_{j=1}^{nr}\frac{\hat{d}_{1i,j}(\omega)}{\hat{d}_{2i,j}(\omega)}, \tag{9}$$

where $N = ns \times nr$ is the total trace number of all shots in each dataset (baseline or monitoring), and $ns$ and $nr$ is the numbers of shots and receivers, respectively. Note, here we assume all shots in the same dataset have the same source wavelet, for the case that have different source waveltes, $f_s(\omega)$ should be calculated shot by shot. Considering the shots in each dataset have the same source wavelet, we replace the subscript pair $(i, j)$ as $k$ and cancel the subscripts of source wavelets representing shot numbers, then re-write equation 9 as:

$$f_s(\omega) = \frac{1}{N}\sum_{k=1}^{N}\frac{\hat{d}_{1k}(\omega)}{\hat{d}_{2k}(\omega)} = \frac{1}{N}\sum_{k=1}^{N}\frac{\hat{w}_1(\omega)\hat{g}_{1k}(\omega)}{\hat{w}_2(\omega)\hat{g}_{2k}(\omega)}, \tag{10}$$

To illustrate $f_s(\omega)$ is a qulified matching filter to reduce the source wavelet nonrepeatibility, we will prove $f_s(\omega) \approx f_w(\omega)$ next. Setting $\delta\hat{g}_k = \hat{g}_{1k} - \hat{g}_{2k}$ associated with the subsurface property change, then equation 10 can be re-written as:

$$f_s(\omega) = \frac{1}{N}\sum_{k=1}^{N}\frac{\hat{w}_1(\omega)(\hat{g}_{2k}(\omega) + \delta\hat{g}_k(\omega))}{\hat{w}_2(\omega)\hat{g}_{2k}(\omega)}. \tag{11}$$

After some algebraic operations, we have:

$$f_s(\omega) = \frac{w_1(\omega)}{w_2(\omega)}(1 + \frac{1}{N}\sum_{k=1}^{N}\frac{\delta\hat{g}_k(\omega)}{\hat{g}_{2k}(\omega)}), \tag{12}$$

where $\delta\hat{g}_k(\omega)$ is the Green's function difference, $\frac{\delta\hat{g}_k(\omega)}{\hat{g}_{2k}(\omega)}$ is the relative Green's function difference, and $\frac{1}{N}\sum_{k=1}^{N}\frac{\delta\hat{g}_k(\omega)}{\hat{g}_{2k}(\omega)}$ is the average of relative Green's function differences. We assume that the average of relative Green's function differences is much smaller than 1 and can be omitted, then we have proved that:

$$f_s(\omega) \approx \frac{w_1(\omega)}{w_2(\omega)} = f_w(\omega). \tag{13}$$

To demonstrate the reasonability of our assumption, a numerical example is employed. In Figure 1, the monitoring Green's function ($\hat{g}_{2k}(\omega)$), the Green's function difference, the relative Green's function difference, and the average of relative Green's function differences are plotted. Models and acquisition parameters used are the same as that in Figure 2 and 4. We observe in Figure 1c and d (or d and h), the relative Green's function difference cannot be ignored for a single trace, its amplitudes are even over 1 sometimes, but the average values of relative Green's function differences in Figure 1d and h are significantly smaller and close to zero (much smaller than 1). Since the relative Green's function differences in different traces can be both negative and positive, they can cancel each other out after averaging. Thus, it is reasonable to omit the average term in equation 12.

The new monitoring data is obtained by multiplying $f_s(\omega)$ with $\hat{d}_{2k}(\omega)$, frequency by frequency, trace by trace. The filter is the same for all traces, but varies with frequency. Note that we are treating baseline data as the reference data which can also be the monitoring data, it depends on the frequency bandwidth of them. The data with a narrower frequency bandwidth should be used as the reference data to avoid errors arising from frequency expansion. Note that, during the calculation of the filter, a damp factor should be designed to avoid the zero-denominator situation. Finally, we convert the new or filtered monitoring data back to time domain by inverse Fourier transfer.

**Fast local cross-correlations and time-shifts correction**

After reducing the source wavelet non-repeatability, we still need to eliminate errors resulting from time shifts between baseline and monitoring data. Even if the two surveys have perfect repeatability, time-shifts correction is essential, since they often cause coherent errors in the final time-lapse imaging. In this subsection, local cross-correlations are calculated to abstract the time shift for each sample.

The cross-correlation between time-domain baseline trace $d_{1k}(t)$ and new monitoring trace $d^{'}_{2k}(t)$ for an integer lag $l$ is defined as follows:

$$c_k[l] = \sum_{i=1}^{Nt} d_{1k}[i]d^{'}_{2k}[i+l] \tag{14}$$

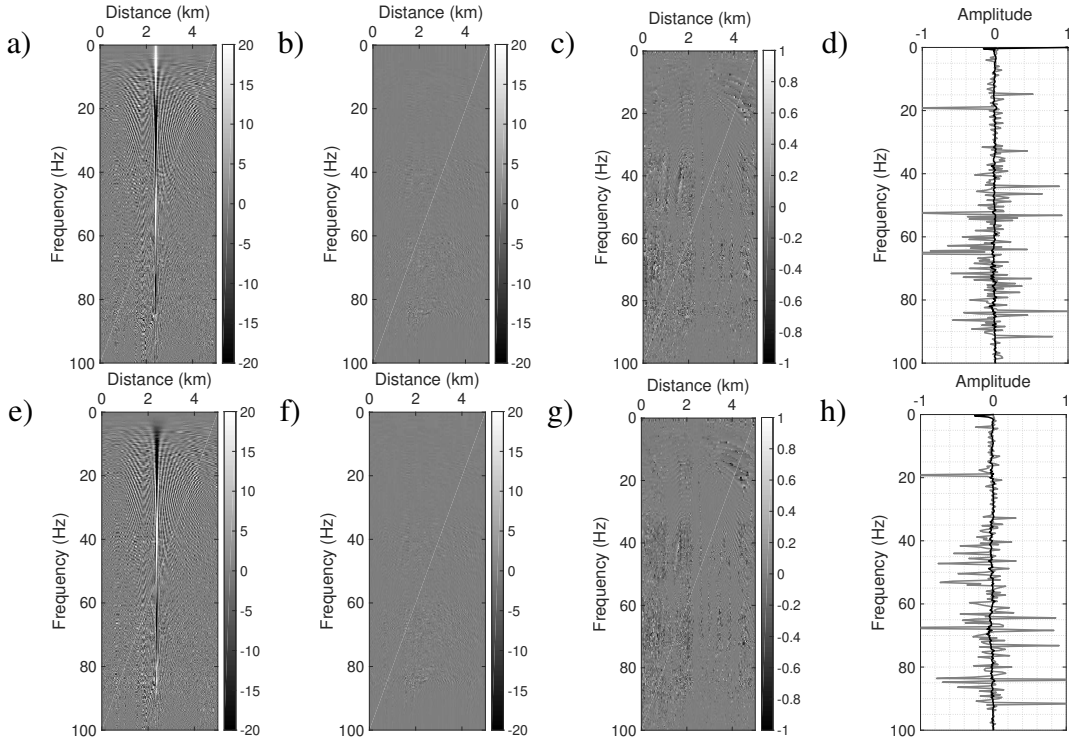


FIG. 1. The real parts of the monitoring Green's function (a), the Green's function difference (b), the relative Green's function difference (c), and the average of relative Green's function differences (the black line in d). Correspondingly, the imaginary parts are plotted in e, f, g, and h. The gray lines in d and h are abstracted from c and g, respectively, at the distance of 2km.

where $d_{1k}[i] = d_{1k}((i-1)\Delta t)$ and $d'_{2k}[i+l] = d'_{2k}((i+l-1)\Delta t)$ represents two discrete sequences, $Nt$ and $\Delta t$ are, respectively, the number of samples of each trace and time sampling interval.

By exploiting Gaussian windows to the sequences, Hale (2006) proposes to calculate the local cross-correlation for each sample, which can be expressed as:

$$C_k[i,l] = \sum_{j=i-Nw/2}^{i+Nw/2} d_{1k}[j] f(j-i) d'_{2k}[j+l] f(j-i+l) \tag{15}$$

Where $f(x) \equiv e^{-x^2/2\sigma^2}$ is a Gaussian function with standard deviation $\sigma$, and $Nw$ denotes the number of non-zero samples in a truncated Gaussian window, i.e., the size of the Gaussian window. Also, Hale (2006) develops a fast algorithm for local cross-correlations calculation, which will be adopted in our work to save computational cost, and it is displayed in $\tilde{Algorithm}1$. For more details on this algorithm, please refer to Hale (2006).

**Algorithm 1:** Fast local cross-correlations (Hale, 2006)

**for** $k \leftarrow 1, 2, \ldots, N$ **do**
  **for** $l \leftarrow -Nl/2, \ldots, Nl/2$ **do** `/* Nl is the number of lags */`
    **for** $i \leftarrow 1, 2, \ldots, Nt$ **do**
      $h[i] \leftarrow d_{1k}[i] \times d^{'}_{2k}[i+l]$
    **end**
    **for** $i \leftarrow 1, 2, \ldots, Nt$ **do** `/* begin shift */`
      $\tilde{h}[i] \leftarrow h[i - l/2]$ `/* interpolate for odd l */`
    **end** `/* end shift */`
    **for** $i \leftarrow 1, 2, \ldots, Nt$ **do** `/* begin Gaussian filter */`
      $C_k[i; l] \leftarrow 0$
      **for** $j \leftarrow i - Nv/2, \ldots, i + Nv/2$ **do** `/*` $Nv \approx Nw/\sqrt{2}$ `*/`
        $C_k[i; l] \leftarrow C_k[i; l] + \tilde{h}[j] \times f(j - i - l/2) \times f(j - i + l/2)$
      **end** `/* end Gaussian filter */`
    **end**
  **end**
**end**

After obtain local cross-correlations for each sample in each trace, we abstract the maximum local cross-correlation in each sample, via:

$$C_{max}[i, k] = \max_{l \in [-Nl/2\ Nl/2]} C_k[i, l], \tag{16}$$

and pick the corresponding lag $l_{max}$. $Nl$ in equation 16 is the number of lags. Finally, the new monitoring trace after time-shift correction can be obtained by:

$$d^{''}_{2k}[i] = d^{'}_{2k}[i + l_{max}]. \tag{17}$$

**Reverse time migration with a Poynting Vector imaging condition**

To display the processed time-lapse data intuitively, we use an RTM to map the shot gathers into reflector imaging in depth. RTM is one of the most used technologies in geophysics, the basic imaging condition used in it is the crosscorrelation imaging condition (Claerbout, 1971; Kaelin and Guitton, 2006):

$$image(x, z) = \sum_t P_f(x, z, t) P_b(x, z, t), \tag{18}$$

where $x$ and $z$ are horizontal and depth coordinations,respectively; $P_f(x, z, t)$ is a forward-propagating wavefield in time from the source location; $P_b(x, z, t)$ is a backward-propagating wavefield in reverse time from receiver locations. For time-lapse imaging, we use the difference data to generate the backward-propagated wavefield.

But equation 18 can not realy represent refletion coefficients of subsurface reflectors, an improvement is normalizing it by the square of the source illumination energy (Claerbout,

1971; Lee et al., 1991; Kaelin and Guitton, 2006), then we have:

$$image(x,z) = \frac{\sum_t P_f(x,z,t)P_b(x,z,t)}{\sum_t P_f(x,z,t)P_f(x,z,t)}. \tag{19}$$

The source-normalized crosscorrelation imaging condition has the same (dimensionless) unit, scaling, and sign as the reflection coefficient (Chattopadhyay and McMechan, 2008).

However, RTM suffers from the imaging of refracted waves, direct waves, and back-scattered waves, which often produce strong artifacts. Although for time-lapse surveys with perfect repeatability, these waves can be eliminated in the difference data, non-repeatability issue is an internal topic. The non-repeatability can cause badly destruction in time-lapse imaging. Especially, small relative errors to strong events (e.g., refracted waves and direct waves) would lead to comparable relative errors to the effective time-lapse signal produced by property changes of the subsurface rock, and make strong coherent errors in time-lapse imaging. We mitigate this problem by using a Poynting Vector imaging condition (Yoon and Marfurt, 2006):

$$image(x,z) = \frac{\sum_t P_f(x,z,t)P_b(x,z,t)W(\cos\theta(x,z,t))}{\sum_t P_f(x,z,t)P_f(x,z,t)}, \tag{20}$$

where

$$\cos\theta(x,z,t) = \frac{\mathbf{v}_f P_f(x,z,t)\cdot \mathbf{v}_b P_b(x,z,t)}{|\mathbf{v}_f P_f(x,z,t)||\mathbf{v}_b P_b(x,z,t)|}, \tag{21}$$

where

$$\mathbf{v}_f = -(\frac{\partial P_f}{\partial x}, \frac{\partial P_f}{\partial z})\frac{\partial P_f}{\partial t},\ \mathbf{v}_b = -(\frac{\partial P_b}{\partial x}, \frac{\partial P_b}{\partial z})\frac{\partial P_b}{\partial t}, \tag{22}$$

$\mathbf{v}_f P_f$ and $\mathbf{v}_b P_b$ are Poynting Vectors of forward- and backward- propagating wavefields, respectively; $\theta(x,z,t)$ is the opening angle (twice of the incident angle); $W(\cos\theta(x,z,t))$ is a weighting factor to rid off values of $image$ over a certain angle range. For example, if we want to keep the values whose incient angle less than $50$ degrees ($100$ degrees opening angle), the $W(\cos\theta(x,z,t))$ may be set to $1$ where $\cos\theta(x,z,t)$ less than $cos(100)$, and $0$ elsewhere. Note that in equation 21 and 22, we use the baseline or monitoring data to obtain the backward-propagating wavefield instead of the difference data used for equations 18, 19 and 20, since the difference data have much lower SNR (signal-to-noise ratio) than baseline or monitoring data, which will lower the quality of calculated incident angles.

## NUMERICAL EXAMPLES

In this section, a modified P-wave Marmousi model and a 2D constant-density acoustic wave equation solved by a finite difference method are used to test our method. A perfectly matched layer (PML) is employed on each side of the model, except the top side on which a free surface is set up. In Figure 2, the baseline model, time-lapse model (monitoring model minus baseline model), smoothing migrated velocity, and geometry are plotted. The model size is 257-by-502, with a 10m grid spacing, 25 sources evenly spread at the top with a 30m depth, and 502 receivers are located at the grids on the surface. A time-lapse velocity change, $4\%$ of the corresponding reservoir velocity, is placed at the center in the baseline model.

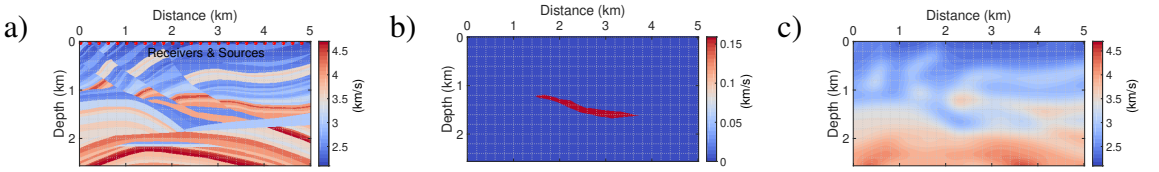


FIG. 2. (a) Baseline model (P-wave velocity); (b) time-lapse model; (c) smoothing migrated velocity model. The dash lines and asterisks in (a) are locations of receivers and sources, respectively.

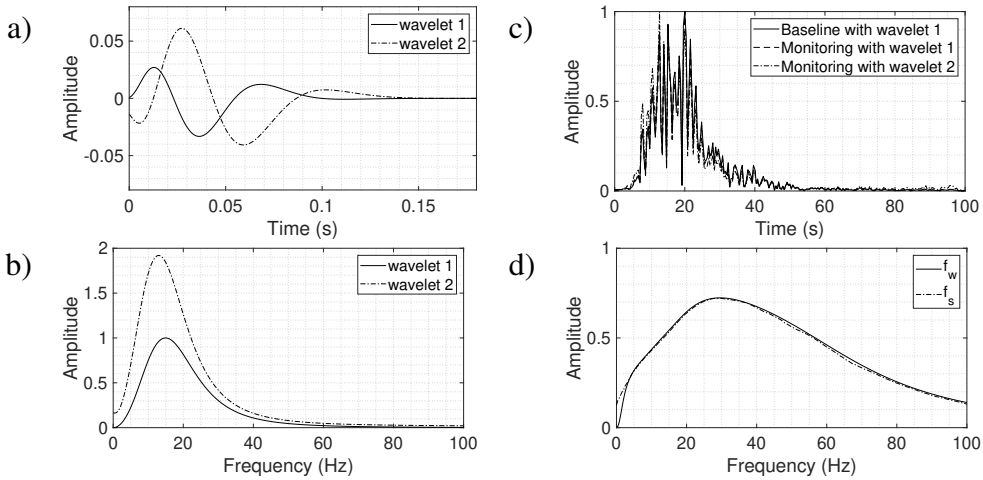


FIG. 3. Two time-domian wavelets (a) and their frequency spectrums (b). (c) Normalized frequency spectrums of a certain baseline and monitoring traces. (d) Calculated frequency-domain filters, $f_w(\omega)$ and $f_s(\omega)$.

## A single-shot gather example

The single-shot gathers are excited at the central source location in Figure 2a. For the case of identical baseline and monitoring wavelets, we use wavelet 1 for both baseline and monitoring surveys, and for the case of different wavelets, we use wavelet 1 for the baseline survey but wavelet 2 for the monitoring survey. And the two wavelets are plotted in Figure 3a-b in both time and frequency domains. Wavelet 1 is a minimum-phase wavelet with a 15Hz peak frequency, and wavelet 2 is a minimum-phase wavelet with a 13Hz peak frequency after amplifying twice and taking a -90-degree phase rotation. Two wavelets are different in peak frequency, maximum amplitude, and phase.

Normalized frequency spectrums of a certain baseline and monitoring traces are plotted in Figure 3c. The normalized-spectrum discrepancy between baseline and monitoring data in the same wavelet case is much smaller than that caused by the wavelet difference. And the filters $f_w(\omega)$, the spectrum ratio of wavelet 1 to wavelet 2, and $f_s(\omega)$ calculated by equation 9 are plotted in Figure 3d. They are close to each other, except when the frequency is smaller than about 3Hz. This is because the average term in equation 12 cannot be ignored at the range of so low frequency, which can also be observed in Figure 1d and h. But this low-frequency error impacts little to the accuracy of $f_s(\omega)$, since the frequency components lower than 3Hz in seismic data are often very weak or lack.

In Figure 4, the difference data are plotted. In Figure 5 and 6, the traces at the distance of 3km in each panel of Figure 4 are plotted. It is observed that $f_w(\omega)$ can almost

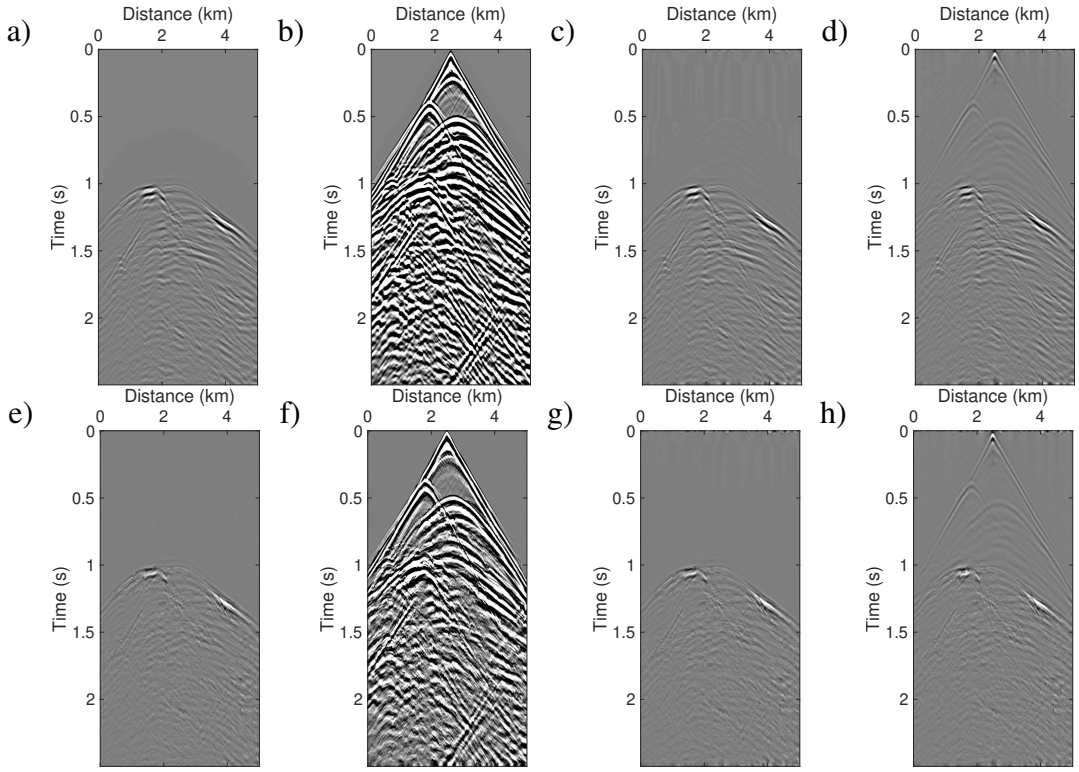


FIG. 4. The difference data before (a,b,c,d) and after (e, f, g, h) implementing the time-shifts correction. (a) Baseline and monitoring wavelets (wavelet 1) are identical. (b) Baseline and monitoring wavelets are different (wavelet 1 for baseline data, wavelet 2 for monitoring data), and there is no processing to both datasets. (c) Baseline and monitoring wavelets are different, but the monitoring data are filtered by $f_w(\omega)$. (d) Baseline and monitoring wavelets are different, but the monitoring data are filtered by $f_s(\omega)$. (e)-(h) are the same as (a)-(d) but having implemented time-shift corrections to monitoring data. All panels are clipped identically.

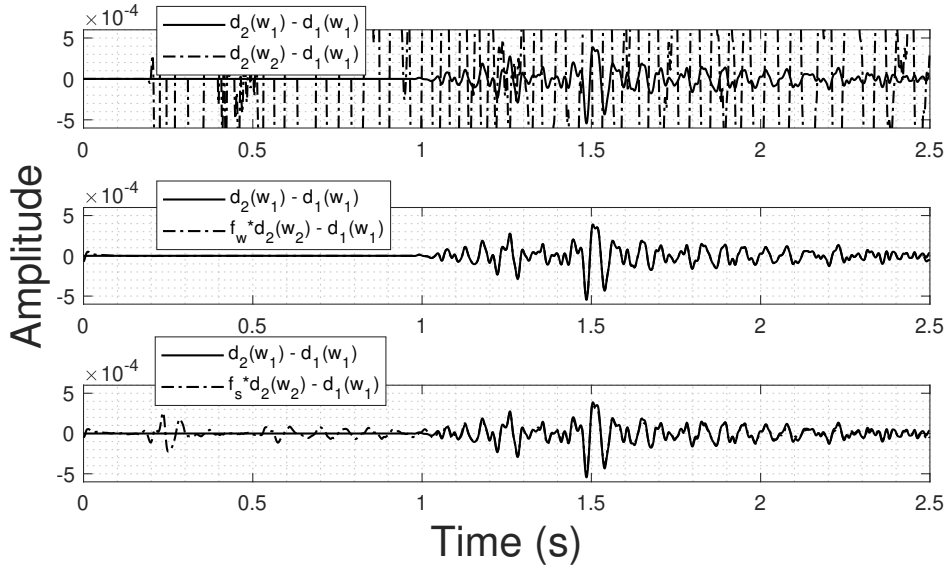


FIG. 5. Traces abstracted from Figure 4a-d at the distance of 3km. All solid lines are identical, which are abstracted from Figure 4a. The dash lines in the first to the third panels are, respectively, abstracted from Figure 4b, c, and d.

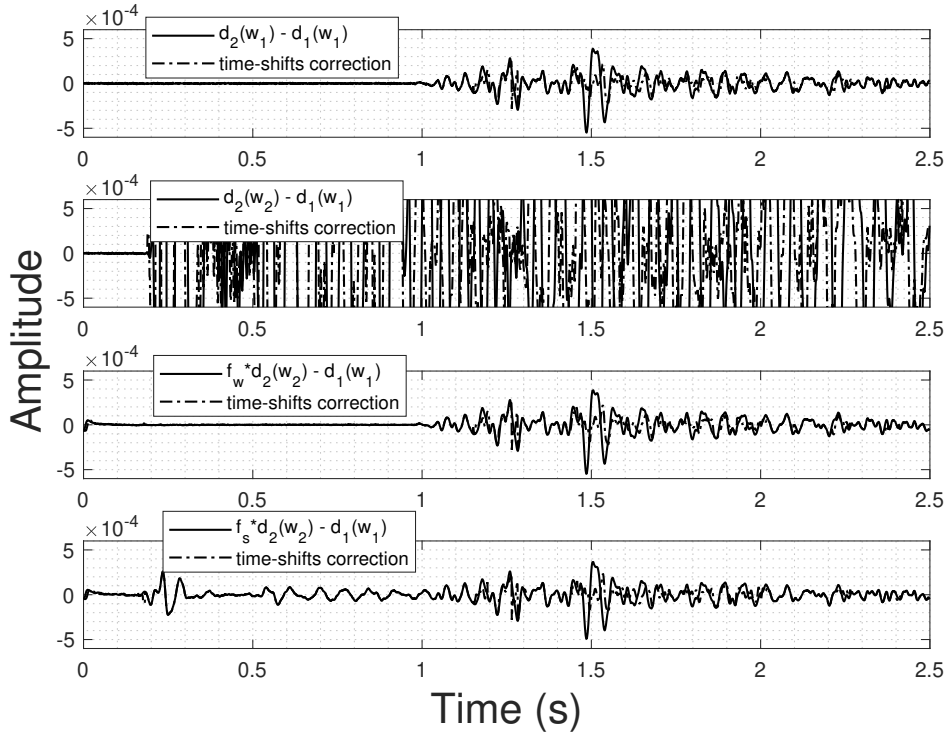


FIG. 6. Traces abstracted from Figure 4a-h at the distance of 3km. The solid lines in the first to the fourth panels are, respectively, abstracted from Figure 4a-d. The dash lines in the first to the fourth panels are, respectively, abstracted from Figure 4e-h.

perfectly eliminate the difference caused by the difference between baseline and monitoring wavelets, and $f_s(\omega)$ also has a fantastic performance on reducing the wavelet non-repeatability. The time-shifts correction based on fast local cross-correlations can effectively attenuate errors resulting from the time shifts between baseline and monitoring data, but it is not really helpful to solve the wavelets non-repeatability issue.The same conclusions can also be observed in Figure 7 and 8 where the difference data in Figure 4a-h are imaged by a RTM.

Furthermore, in Figure 7 and 8, we observe using $f_w(\omega)$ can produce imaging almost the same as that with perfect wavelet repeatability. And using $f_s(\omega)$ still has some remain coherent errors mainly above the time-lapse change, which can also be observed in Figure 4d and the third panel of Figure 5. Using the Poynting Vector imaging condition (Figure 7e) can effectively decrease these errors. The RTM imagings after time-shifts corrections are plotted in Figure 8, in which we observe that time-shifts corrections can reduce artifacts, especially, that closely beneath the events representing the time-lapse change. This is significant to mitigate incorrect interpretation of the time-lapse change.

However, we can still see errors outside the time-lapse area in 8c and e. They come at least from the following aspects: (1) the remaining time shifts; (2) the amplitude changes of waves caused by the sencond or higher-order scattering of time-lapse change; (3) the inaccurate velocity using for RTM imaging; (4) the inaccuracy of $f_s(\omega)$ for Figure 8e.

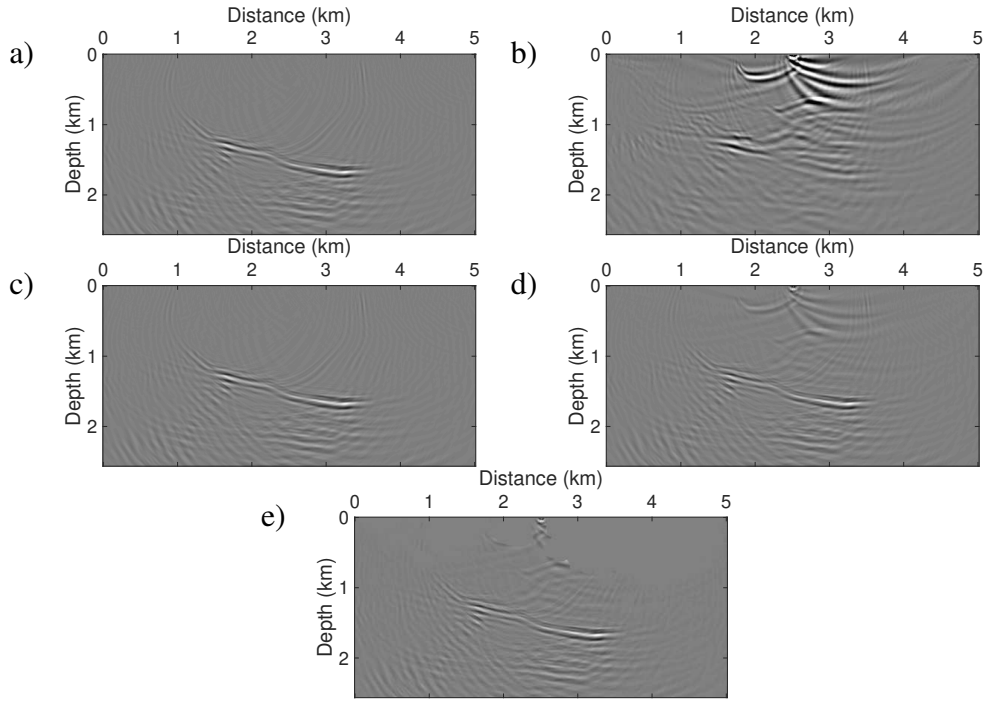


FIG. 7. The RTM imagings of the difference data before time-shifts correction in Figure 4a-d. (a)-(d) are, respectively, imagings of Figure 4a-d with the source-normalized imaging condition (equation 19). (e) is the imaging of Figure 4d with the Poynting Vector imaging condition (equation 20), and the incident angles are limited within $50$ degrees.

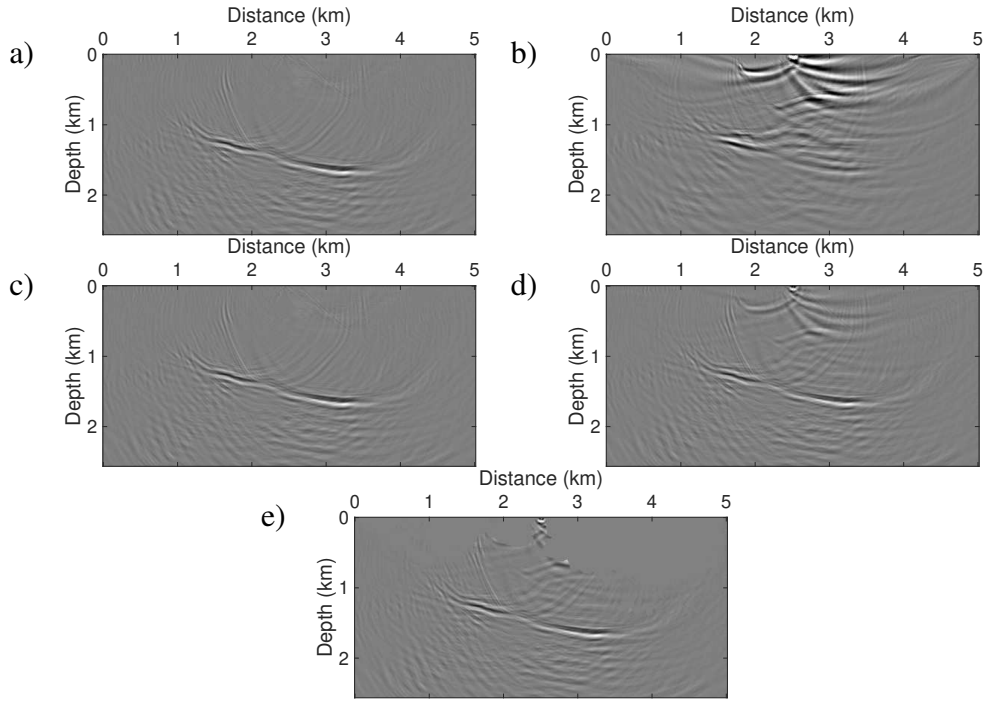


FIG. 8. The RTM imagings of the difference data after time-shifts correction in Figure 4e-h. (a)-(d) are, respectively, imagings of Figure 4e-h with the source-normalized imaging condition (equation 19). (e) is the imaging of Figure 4h with the Poynting Vector imaging condition (equation 20), and the incident angles are limited within $50$ degrees.

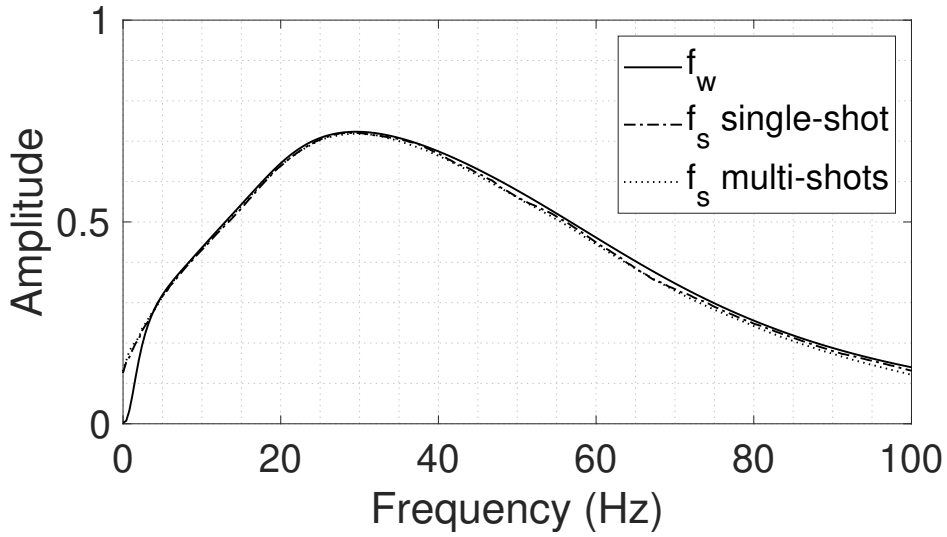


FIG. 9. The solid and dash lines are the same as that in Figure 3d, the former is calculated from the wavelets spectrums and the latter is calculated from the single-shot gathers. The dot line is $f_s(\omega)$ calculated from all shots.

**Multi-shot gathers examples**

Here, we use all shots, including 25 baseline shots and 25 monitoring shots, to test our methods, and all shots are excited one by one with wavelet 1 for baseline survey and wavelet 2 for monitoring survey.

*Noise-free data tests*

In Figure 9, the source-independent matching filters $f_s(\omega)$, calculated from the central shots and all shots of noise-free datasets, and $f_w(\omega)$ are plotted. It is observed that $f_s(\omega)$ calculated from all shots has similar accuracy to that calculated from the central shots, both of them are close to $f_w(\omega)$ but with a bias when the frequency is lower than about 3Hz.

In Figure 10 and 11, the RTM imagings of the difference data before (Figure 10) and after (Figure 11) time-shifts corrections using all shots with the source-normalized imaging condition and the Poynting Vector imaging condition are plotted. Similarly to that in Figure 7 and 8, we can see a significant improvement after using $f_w(\omega)$ or $f_s(\omega)$. Also, we observe that time-shifts corrections calibrate the three events (two dark ones and a bright one) to two events (a dark one and a bright one) in the time-lapse area that is more accurate. And the Poynting Vector imaging condition can reduce the artifacts above the time-lapse area, especially, in the shallow part.

*Noisy data tests*

We test our method using data with SNR (signal-to-noise ratio) equals to 2 and 1. The same-level but non-repeatable Gaussian random noises are added to noise-free baseline and monitoring data separately. The central noisy baseline shots and corresponding difference data are displayed in Figure 12 where a sharp SNR decrease in the difference data can be

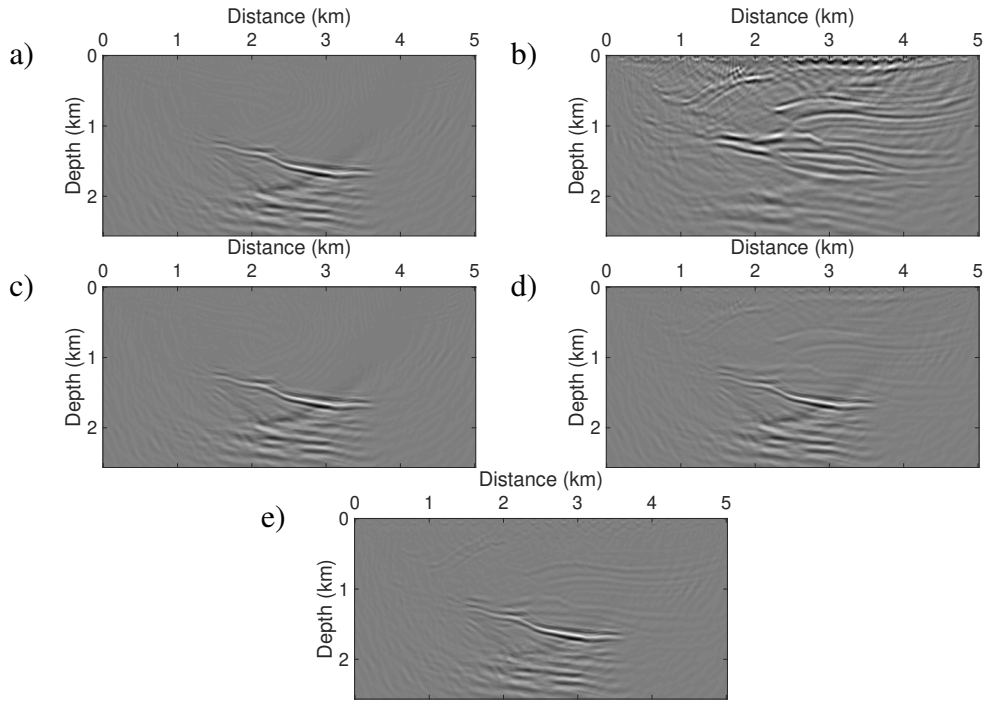


FIG. 10. The RTM imagings of the difference data before time-shifts corrections using all 25 shots with (a)-(d) the source-normalized imaging condition or (e) the Poynting Vector imaging condition in which the incident angles are limited within $50$ degrees. (a) Baseline and monitoring wavelets are identical. (b) Baseline and monitoring wavelets are different, and monitor data are not processed. (c) Baseline and monitoring wavelets are different, and monitor data are filtered by $f_w$. (d) and (e) Baseline and monitoring wavelets are different, and monitor data are filtered by $f_s$.

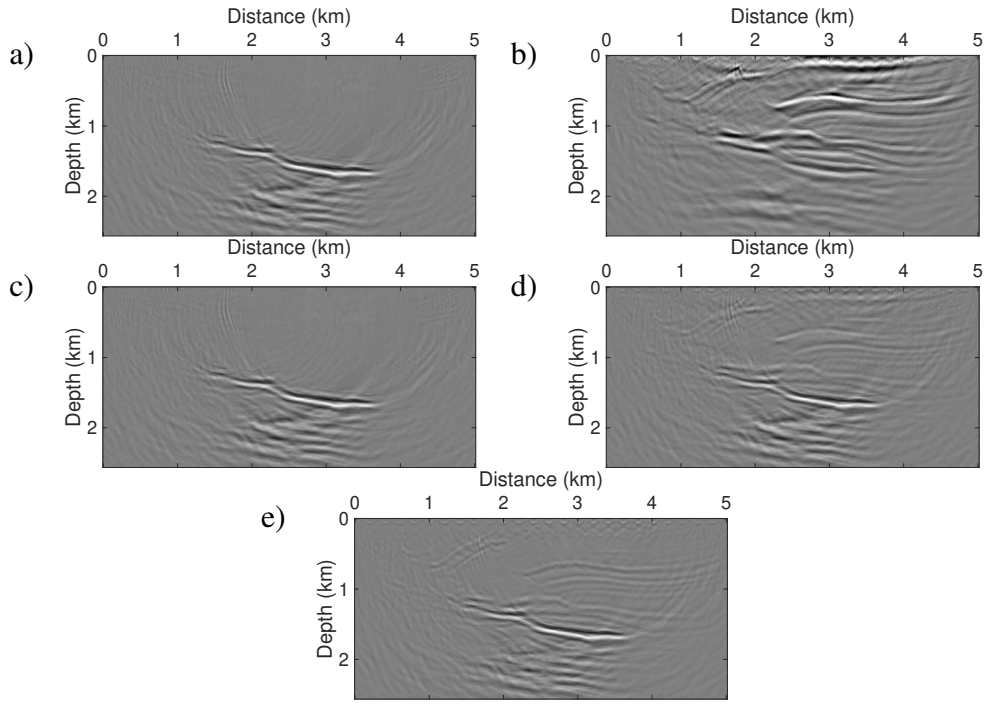


FIG. 11. The RTM imagings of the difference data after time-shifts corrections using all 25 shots with (a)-(d) the source-normalized imaging condition or (e) the Poynting Vector imaging condition in which the incident angles are limited within $50$ degrees. (a) Baseline and monitoring wavelets are identical. (b) Baseline and monitoring wavelets are different, and monitor data are not processed. (c) Baseline and monitoring wavelets are different, and monitor data are filtered by $f_w$. (d) and (e) Baseline and monitoring wavelets are different, and monitor data are filtered by $f_s$.

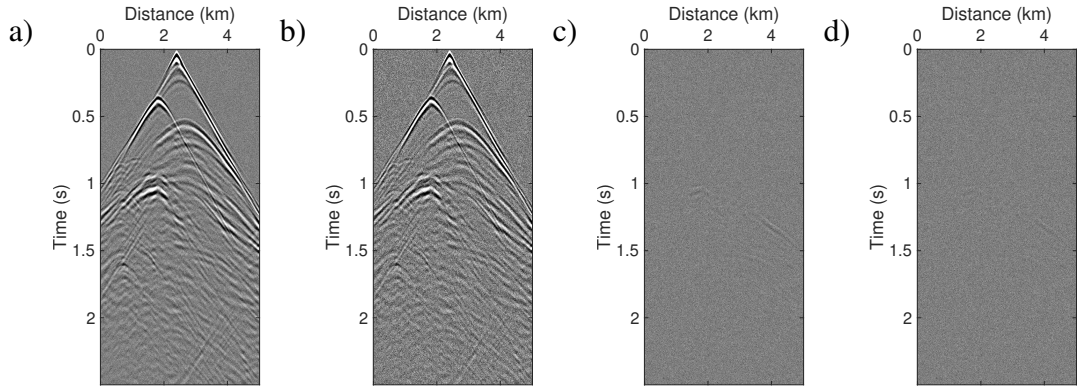


FIG. 12. The central shots of baseline data with SNR=2 (a) and SNR=1 (b). The difference data of the central shots with SNR=2 (c) and SNR=1 (d).

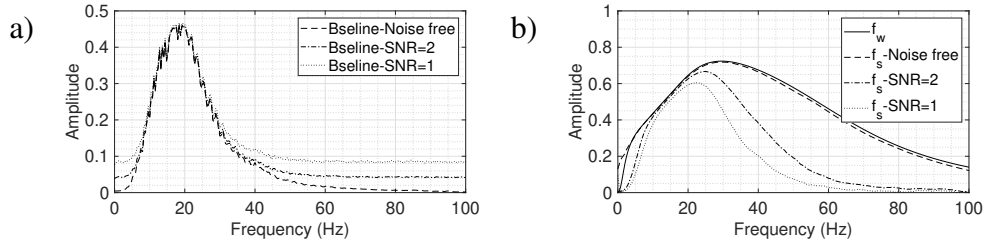


FIG. 13. (a) Average frequency spectrums of the central shot of noise-free and noisy baseline data.(b) Calculated matching filters for noise-free and noisy data.

observed.

In Figure 14, Average frequency spectrums of the central shot of noise-free and noisy baseline data are plotted, as well as the calculated matching filters ($f_w(\omega)$ and $f_s(\omega)$) for noise-free and noisy data. We observe, with the noise level increasing, the source-independent matching filter ($f_s(\omega)$) becomes worse, and the most accurate segment occurs near the peak frequency (from about 10Hz to 20Hz) since these frequencies are less destroyed by noises.

The RTM imagings of the noisy difference data, including all 25 shots after time-shifts correction, using the source-normalized imaging condition (equation 19) and the Poynting Vector imaging condition (equation 20) are plotted in Figure 14 and 15. For the data with SNR=2, we can still clearly recognize the time-lapse area from the imagings using $f_s(\omega)$, but for the data with SNR=1, $f_s(\omega)$ does not work well. And the performs of $f_w(\omega)$ are very stable for data with different noise levels. Additionally, $f_w(\omega)$ can function as decreasing the random noise since it is a band-pass filter essentially. The Poynting Vector imaging condition can significantly suppress the shallow-part coherent errors in noisy data imagings.

## CONCLUSIONS

We have developed two frequency-domain matching filters to reduce source wavelet non-repeatability, one is the spectrum ratio of the baseline and monitoring wavelets, the other is the average spectrum ratio of the baseline and monitoring traces. The former requires the wavelets information of baseline and monitoring data, and the latter is source-

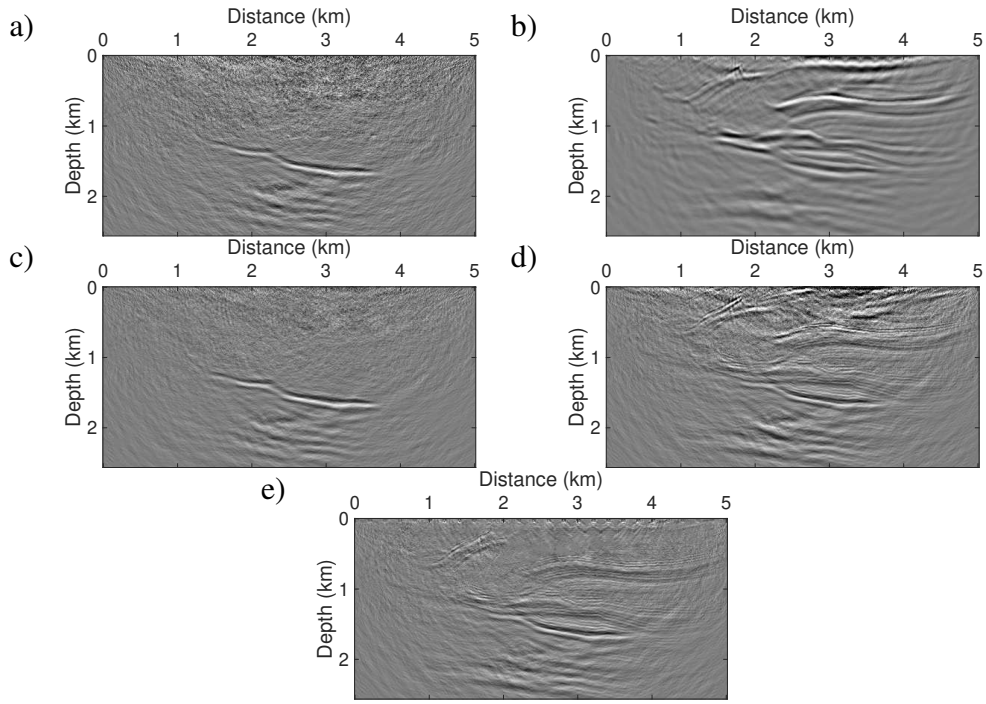


FIG. 14. The RTM imagings of the difference data (SNR=2) after time-shifts corrections using all 25 shots with (a)-(d) the source-normalized imaging condition or (e) the Poynting Vector imaging condition in which the incident angles are limited within $50$ degrees. (a) Baseline and monitoring wavelets are identical. (b) Baseline and monitoring wavelets are different, and monitor data are not processed. (c) Baseline and monitoring wavelets are different, and monitor data are filtered by $f_w$. (d) and (e) Baseline and monitoring wavelets are different, and monitor data are filtered by $f_s$.

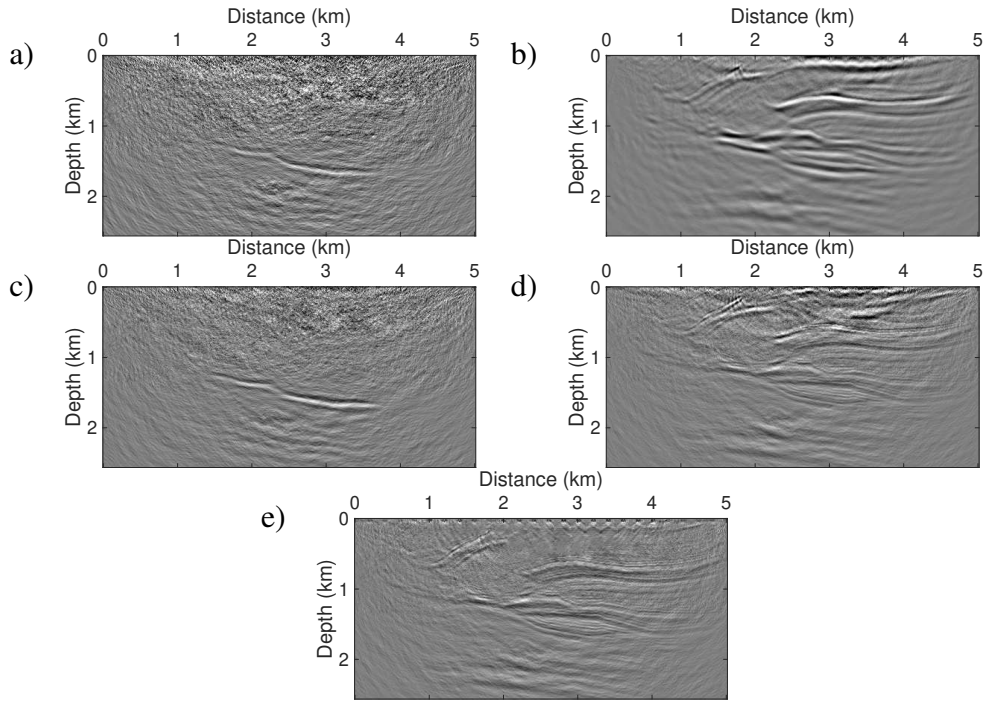


FIG. 15. The RTM imagings of the difference data (SNR=1) after time-shifts corrections using all 25 shots with (a)-(d) the source-normalized imaging condition or (e) the Poynting Vector imaging condition in which the incident angles are limited within $50$ degrees. (a) Baseline and monitoring wavelets are identical. (b) Baseline and monitoring wavelets are different, and monitor data are not processed. (c) Baseline and monitoring wavelets are different, and monitor data are filtered by $f_w$. (d) and (e) Baseline and monitoring wavelets are different, and monitor data are filtered by $f_s$.

independent.

After reducing the source wavelet non-repeatability, we have employed a time-shifts correction by a fast local cross-correlations algorithm to further reduce the non-repeatability caused by time shifts in the difference data. And an RTM in depth with a Poynting Vector imaging condition has been used to reduce the remaining errors arising from the inaccuracy of the source-independent matching filter.

The feasibility of our methods has been demonstrated by the synthetic noise-free and noisy data tests. The spectrum ratio of the baseline and monitoring wavelets have shown fantastic performances during these tests. The source-independent filter, with a certain anti-noise ability, can also effectively solve the problem of non-repeatability of source wavelets. But high-quality shot gathers are still the guarantee of the success of the source-independent method.

## DISCUSSION

In cross-equalization Rickett and Lumley (2001), processing for solving source wavelet non-repeatability issue is also included, it comprises steps: (1) Picking a window above the reservoir zone where the time-lapse change; (2) calculating the spectral balancing filter or the time-domain least-squares filter using the data in the window for each trace; (3) applying each filter to the corresponding trace as a whole. This processing can be employed in both shot gathers and CDP (common depth point) data. But positioning the reservoir in shot gathers is not an easy thing and the first arrivals could also take the information about the reservoir. Also, since wavelets in CDP data are variable vertically (temporally) and horizontally (spacially), after performing the cross-equalization the eliminating remaining wavelet non-repeatability errors are still challenging (Rickett and Lumley, 2001). Furthermore, performing the filtering trace-by-trace is not good for anti-noise.

In our work, we focus on the source wavelet non-repeatability issue. In practice, more non-repeatability issues should be considered, for example, before using the matching filters in this paper, the baseline and monitoring shot gathers should be interpolated and resampled into the same grids, and denoising and low-pass filtering can also be used, which do not change the relationship in equation 2. Additionally, we have assumed that the source locations are identical in the two surveys. We believe our methods are also applicable for elastic shot gathers that can also be expressed as convolutions between wavelets and Green's functions, and they can also be used in 4D (or time-lapse) full-waveform inversion where the raw shot gathers are used.

## ACKNOWLEDGEMENTS

We thank the sponsors of CREWES for continued support. This work was funded by CREWES industrial sponsors, NSERC (Natural Science and Engineering Research Council of Canada) through the grants CRDPJ 543578-19. Partial funding also came from the Canada First Research Excellence Fund.

## REFERENCES


Al-Ismaili, I. Y., and Warner, M. R., 2002, Non-linear cross-equalization of time-lapse seismic surveys using artificial neural networks, *in* 64th EAGE Conference & Exhibition, European Association of Geoscientists & Engineers, cp–5.

Almutlaq, M. H., and Margrave, G. F., 2013, Surface-consistent matching filters for time-lapse seismic processing: Geophysics, **78**, No. 5, M29–M41.

Arts, R., Eiken, O., Chadwick, A., Zweigel, P., Van der Meer, L., and Zinszner, B., 2003, Monitoring of co2 injected at sleipner using time lapse seismic data, *in* Greenhouse Gas Control Technologies-6th International Conference, Elsevier, 347–352.

Barkved, O., Buer, K., Halleland, K., Kjelstadli, R., Kleppan, T., and Kristiansen, T., 2003, 4d seismic response of primary production and waste injection at the valhall field, *in* 65th EAGE Conference & Exhibition, European Association of Geoscientists & Engineers, cp–6.

Barkved, O. I., Kristiansen, T., and Fjær, E., 2005, The 4d seismic response of a compacting reservoir—examples from the valhall field, norway, *in* SEG Technical Program Expanded Abstracts 2005, Society of Exploration Geophysicists, 2508–2511.

Bergmann, P., Kashubin, A., Ivandic, M., Lüth, S., and Juhlin, C., 2014, Time-lapse difference static correction using prestack crosscorrelations: 4d seismic image enhancement case from ketzin: Geophysics, **79**, No. 6, B243–B252.

Chadwick, R., Noy, D., Arts, R., and Eiken, O., 2009, Latest time-lapse seismic data from sleipner yield new insights into co2 plume development: Energy Procedia, **1**, No. 1, 2103–2110.

Chattopadhyay, S., and McMechan, G. A., 2008, Imaging conditions for prestack reverse-time migration: Geophysics, **73**, No. 3, S81–S89.

Claerbout, J. F., 1971, Toward a unified theory of reflector mapping: Geophysics, **36**, No. 3, 467–481.

Dramsch, J. S., Christensen, A. N., MacBeth, C., and Lüthje, M., 2019, Deep unsupervised 4d seismic 3d time-shift estimation with convolutional neural networks.

Fomel, S., 2007, Local seismic attributes: Geophysics, **72**, No. 3, A29–A33.

Fomel, S., and Jin, L., 2009, Time-lapse image registration using the local similarity attribute: Geophysics, **74**, No. 2, A7–A11.

Fu, X., Romahn, S., and Innanen, K., 2020, Double-wavelet double-difference time-lapse waveform inversion, *in* SEG Technical Program Expanded Abstracts 2020, Society of Exploration Geophysicists, 3764–3767.

Gallop, J., 2011, Midpoint match filtering, *in* SEG Technical Program Expanded Abstracts 2011, Society of Exploration Geophysicists, 4170–4174.

Greaves, R. J., and Fulp, T. J., 1987, Three-dimensional seismic monitoring of an enhanced oil recovery process: Geophysics, **52**, No. 9, 1175–1187.

Hale, D., 2006, Fast local cross-correlations of images, *in* SEG Technical Program Expanded Abstracts 2006, Society of Exploration Geophysicists, 3160–3164.

Hale, D., 2009, A method for estimating apparent displacement vectors from time-lapse seismic images: Geophysics, **74**, No. 5, V99–V107.

Hale, D., 2013, Dynamic warping of seismic images: Geophysics, **78**, No. 2, S105–S115.

Hall, S. A., MacBeth, C., Barkved, O. I., and Wild, P., 2005, Cross-matching with interpreted warping of 3d streamer and 3d ocean-bottom-cable data at valhall for time-lapse assessment: Geophysical Prospecting, **53**, No. 2, 283–297.

Hatchell, P., and Bourne, S., 2005, Measuring reservoir compaction using time-lapse timeshifts, *in* SEG Technical Program Expanded Abstracts 2005, Society of Exploration Geophysicists, 2500–2503.

Hatchell, P., and Tatanova, M., 2019, Matching of 4d seismic data: Spectrum balancing vs conventional least squares filters, *in* SEG Technical Program Expanded Abstracts 2019, Society of Exploration Geophysicists, 5245–5249.

Hicks, E., Hoeber, H., Houbiers, M., Lescoffit, S. P., Ratcliffe, A., and Vinje, V., 2016, Time-lapse full-waveform inversion as a reservoir-monitoring tool—a north sea case study: The Leading Edge, **35**, No. 10, 850–858.

Jack, I., 2017, 4d seismic—past, present, and future: The Leading Edge, **36**, No. 5, 386–392.

Kaelin, B., and Guitton, A., 2006, Imaging condition for reverse time migration, *in* SEG Technical Program Expanded Abstracts 2006, Society of Exploration Geophysicists, 2594–2598.

Karimi, P., Fomel, S., and Zhang, R., 2016, Time-lapse image registration using the stratigraphic-coordinate system, *in* SEG Technical Program Expanded Abstracts 2016, Society of Exploration Geophysicists, 5500–5505.

Kazemeini, S. H., Juhlin, C., and Fomel, S., 2010, Monitoring co2 response on surface seismic data; a rock physics and seismic modeling feasibility study at the co2 sequestration site, ketzin, germany: Journal of Applied Geophysics, **71**, No. 4, 109–124.

Lee, D., Mason, I. M., and Jackson, G. M., 1991, Split-step fourier shot-record migration with deconvolution imaging: Geophysics, **56**, No. 11, 1786–1793.

Liu, X., Chen, X., Bai, M., and Chen, Y., 2021, Time-lapse image registration by high-resolution time-shift scan: Geophysics, **86**, No. 3, M49–M58.

Lumley, D. E., 2001, Time-lapse seismic reservoir monitoring: Geophysics, **66**, No. 1, 50–53.

Pevzner, R., Urosevic, M., Popik, D., Shulakova, V., Tertyshnikov, K., Caspari, E., Correa, J., Dance, T., Kepic, A., Glubokovskikh, S. et al., 2017, 4d surface seismic tracks small supercritical co2 injection into the subsurface: Co2crc otway project: International Journal of Greenhouse Gas Control, **63**, 150–157.

Phillips, M., and Fomel, S., 2016, Seismic time-lapse image registration using amplitude-adjusted plane-wave destruction, *in* SEG Technical Program Expanded Abstracts 2016, Society of Exploration Geophysicists, 5473–5478.

Rickett, J., and Lumley, D., 2001, Cross-equalization data processing for time-lapse seismic reservoir monitoring: A case study from the gulf of mexico: Geophysics, **66**, No. 4, 1015–1025.

Ross, C., Cunningham, G., and Weber, D., 1996, Inside the crossequalization black box: The Leading Edge, **15**, No. 11, 1233–1240.

Ross, C. P., and Altan, M. S., 1997, Time-lapse seismic monitoring: Some shortcomings in nonuniform processing: The Leading Edge, **16**, No. 6, 931–937.

Tucker, B., Hoover, A. R., and Flemings, P. B., 2000, Time-lapse (4-d) seismic monitoring of primary production of turbidite reservoirs at south timbalier block 295, offshore louisiana, gulf of mexico: Geophysics, **65**, No. 2, 351–367.

Wang, Z., Cates, M. E., and Langan, R. T., 1998, Seismic monitoring of a co2 flood in a carbonate reservoir: A rock physics study: Geophysics, **63**, No. 5, 1604–1617.

Williamson, P., Cherrett, A., and Sexton, P., 2007, A new approach to warping for quantitative time–lapse characterisation, *in* 69th EAGE Conference and Exhibition incorporating SPE EUROPEC 2007, European Association of Geoscientists & Engineers, cp–27.

Yoon, K., and Marfurt, K. J., 2006, Reverse-time migration using the poynting vector: Exploration Geophysics, **37**, No. 1, 102–107.